SPACE WEATHER, VOL. 1, NO. 3, 1014, doi:10.1029/2003SW000023, 2003

Precursor analysis and prediction of large-amplitude relativistic electron fluxes

R. S. Weigel
Laboratory for Atmospheric and Space Physics, University of Colorado, Boulder, Colorado, USA

A. J. Klimas
NASA Goddard Space Flight Center, Greenbelt, Maryland, USA

D. Vassiliadis
Universities Space Research Association at NASA Goddard Space Flight Center, Greenbelt, Maryland, USA

Received 18 August 2003; revised 11 September 2003; accepted 24 September 2003; published 12 December 2003.

[1] An analysis of large-amplitude relativistic electron fluxes, J_e, is given using models that predict their appearance based on solar wind precursors. It has been noted that relativistic electron flux bursts in the magnetosphere are associated with high-speed solar wind streams. This observation is used to motivate several models that quantify the association in terms of 2 × 2 contingency tables. For each model, the minimal cost structure for which the model would be useful is computed as a function of large threshold values of J_e. The first model is based on the observation that a threshold crossing in the daily averaged solar wind velocity, V_{SW}, tends to precede large relativistic electron fluxes. The optimal ratio of correct to false alarms forecasts found using this algorithm is 18:4 for a threshold corresponding to amplitudes of J_e at $L = 4.4$ above $J_c = 10^3$ particles/str·cm^2·s (corresponding to 110 total events). The second model allows for jumps in the solar wind to be an event indicator and yields slight improvements in the forecast ratio for larger values of J_c. The dependence of the optimal forecast ratio on L shell is also considered. It is shown that there are L values for which a threshold crossing of the daily average of V_{SW} from below to above 600 km/sec is a sufficient condition for the appearance of large-amplitude relativistic electron fluxes on one of the following three days. It is also shown that the condition of a threshold crossing of V_{SW} above 600 km/s is not a necessary condition, because ≃80% of events were not preceded by this condition. *INDEX TERMS:* 2722 Magnetospheric Physics: Forecasting; 2740 Magnetospheric Physics: Magnetospheric configuration and dynamics; 2784 Magnetospheric Physics: Solar wind/magnetosphere interactions; 2720 Magnetospheric Physics: Energetic particles, trapped; *KEYWORDS:* MeV electrons, event prediction, precursor analysis

Citation: Weigel, R. S., A. J. Klimas, and D. Vassiliadis, Precursor analysis and prediction of large-amplitude relativistic electron fluxes, *Space Weather*, *1*(**3**), 1014, doi:10.1029/2003SW000023, 2003.

1. Introduction

[2] A moderate correlation between the solar wind velocity, V_{SW}, or a prediction filter of V_{SW}, and the log of the relativistic electron flux, $\log(J_e)$, has been shown. At geosynchronous altitudes ($6.6R_E$) the peak cross-correlation between daily averages of V_{SW} and $\log(J_e)$ is 0.4 at a time lag of 3 days [*Baker et al.*, 1990; *Vassiliadis et al.*, 2002]. A linear moving average filter of V_{SW} can explain ~50% of the variance in $\log(J_e)$ on a 1-day time scale [*Baker et al.*, 1990; *Vassiliadis et al.*, 2002], and comparable results are obtained using a semiempirical model [*Li et al.*, 2001]. These models capture some of the driving of $\log(J_e)$ by high-speed solar wind streams, which often precede large increases in the flux of relativistic electrons in the magnetosphere [*Baker et al.*, 1998].

[3] Substantial energetic electron damage to satellites usually only occurs when the integrated relativistic electron flux is very large [*Baker et al.*, 1987; *Vampola*, 1987]. Thus for forecasting purposes it is important to predict whether there will be a large J_e (an "event") on a given day in the future, in addition to predicting the day-to-day amplitude of $\log(J_e)$. Models that specify a day-to-day value of $\log(J_e)$ based on past solar wind velocity measurements can be used to predict large events. However, a model optimized to have a high day-to-day data-model correlation between V_{SW} and $\log(J_e)$ will not necessarily be an optimal predictor of a large event in J_e.

[4] In this work we take a direct approach in predicting when the relativistic electron flux will exceed a threshold value. When a function of past measurements of the solar wind velocity crosses a threshold value, a prediction of a threshold crossing in J_e is made. The event-forecast function is optimized to have the largest ratio of the number of correct event forecasts to the number of incorrect event forecasts, which is a prediction quality metric appropriate for evaluating an event forecast from a user's perspective [*Thomson*, 2000].

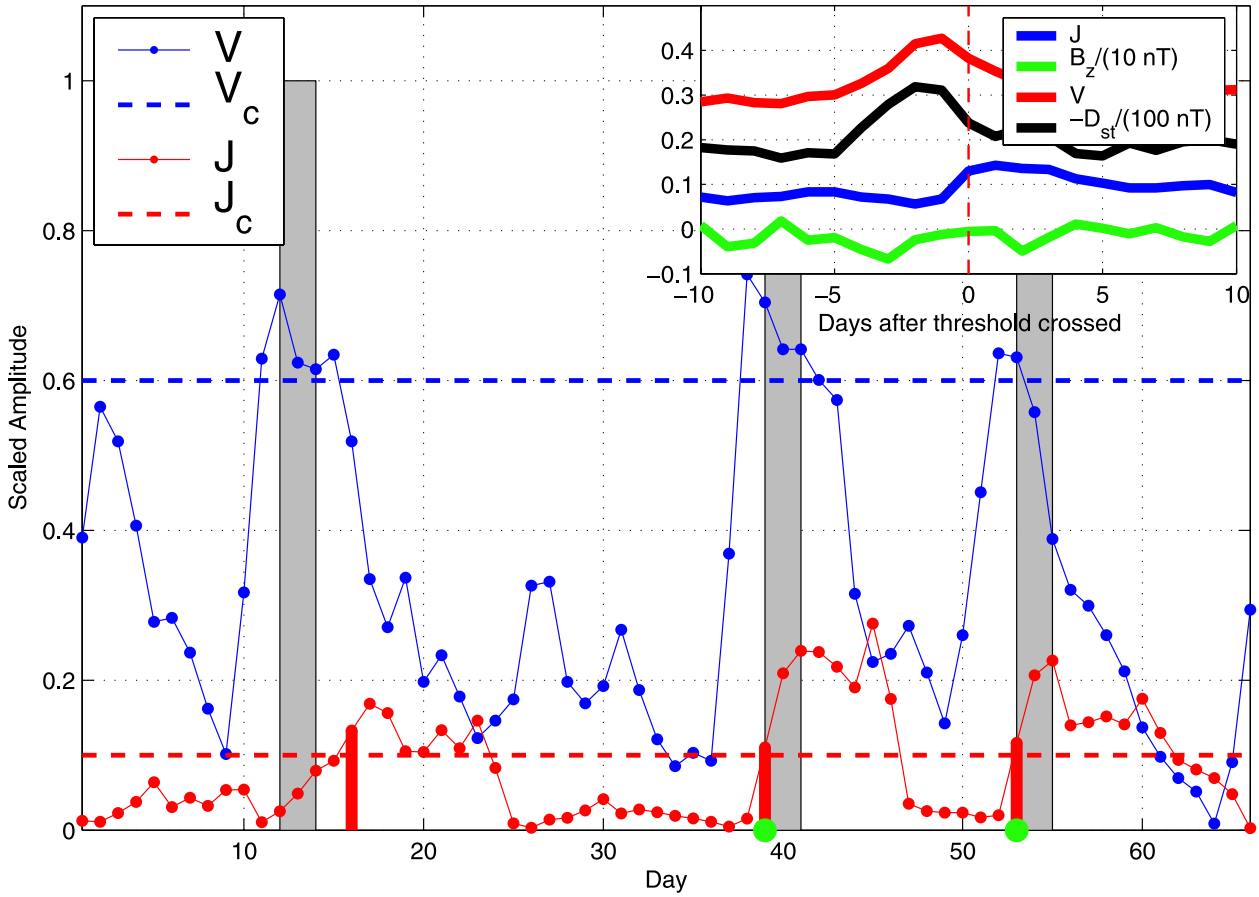

Figure 1. Vertical shaded bars mark t_F, $t_F + 1$, or $t_F + 2$, the days when an event is forecast. Vertical red lines mark t_E, the day of an event in J. A correctly forecasted event in J is marked with a green dot on the abscissa. The inset includes averages of time series around the day of threshold crossing in J.

[5] High-speed streams have a characteristic velocity feature; typically, over one day the solar wind velocity increases from a value of 400 km/s or less to a value of 500 km/s or more, and its amplitude remains high over several days. We test several forecast algorithms that are based on and quantify the value of this observation as a predictor. The first forecast scheme states that if V_{SW} on day $t - 2$ was less than a threshold value V_c and V_{SW} on day $t - 1$ is greater than V_c, an event is forecasted on days t, $t + 1$, and $t + 2$. The second model considered allows an event to be predicted if there is a large jump in the solar wind velocity. Finally, the dependence of the threshold model performance is evaluated in the range L = [1.1, 10].

2. Forecast Algorithm

[6] We first consider a simple forecast algorithm to assess how reliably changes in the solar wind velocity can be used to predict increases in the relativistic electron flux at L = 4.4. This position was chosen because it corresponds to the value for which the impulse response of J_e to V_{SW} is the largest [*Vassiliadis et al.*, 2002]. The algorithm uses the two prior daily averages of V_{SW} to make a forecast on a given day. This algorithm is motivated by the observed association between elevated V_{SW} and large increases in log(J_e) [*Blake et al.*, 1997; *Baker et al.*, 1997; *O'Brien et al.*, 2001; *Vassiliadis et al.*, 2003]. That is, given an event in log(J_e), there is generally an elevated V_{sw} on the days preceding. For a precursor analysis, we need to determine how often this solar wind signature will yield an event in J_e.

[7] Correlation analysis or epoch analysis centered on the time of an energetic electron event can reveal an association between an event and a driver. The inset of Figure 1 shows the epoch averages of V_{sw}, D_{st}, and B_z with zero time corresponding to the first day for which J_e was above a large threshold. To assess the value of such an association as a precursor, one must consider the probability of observing an event given a condition in the solar wind *before* the energetic electron event. In the language of Bayesian statistics, the posterior probability P(Event|Con-Condition) must be calculated; the posterior cannot be reconstructed from epoch or correlation analysis, which yields P(Average Condition|Event).

[8] The daily averaged J_e data in the energy range of 2–6 MeV were obtained from the Proton Electron Telescope on the Solar Anomalous and Magnetospheric Particle Explorer (SAMPEX) spacecraft. The daily averaged solar wind data from WIND and the Advanced Composition Explorer (ACE) were obtained from the OMNIWeb database. The full data set consists of 1950 values of $V_{sw}(t)$ and $J_e(t, L)$ at an L shell resolution of 0.1 beginning on day 285 of 1994. Note that we are using the daily averaged flux as a proxy for the integrated flux, which is the quantity that is more closely related to satellite failure; with the use of subdaily data, an improved integrated flux quantity should be possible.

[9] The scaled velocity V is defined as

$$V(t) = \frac{V_{\mathrm{SW}}(t) - V_{\mathrm{SW\ min}}}{V_{\mathrm{SW\ max}} - V_{\mathrm{SW\ min}}}, \tag{1}$$

where $V_{\mathrm{SW\ min}}$ = 263 km/s and $V_{\mathrm{SW\ max}}$ = 824 km/s are the minimum and maximum values of V_{SW} in the data set, while the average value is 350 km/s. The scaled flux is defined by $J \equiv J_e/J_o$, with J_o = 1000 particles/str·cm^2·s.

[10] A threshold crossing event E on day t_E is defined as any t_E for which $J(t_E - 1) \leq J_c$ and $J(t_E) > J_c$, where J_c is an adjustable threshold parameter. The set of t_E values is found from a search of the J time series. The first algorithm forecasts an event in J on any day t_F for which the set of rules

$$V(t_F - 1) \geq V_c \text{ and } V(t_F - 2) < V_c \text{ and } J(t_F - 1) < J_c \tag{2}$$

is satisfied, where V_c is an adjustable velocity threshold parameter. The first rule, $J(t_F - 1) < J_c$, prevents a forecast from being made when J is already above the threshold value. The times t_F that satisfy the above set of rules are obtained from evaluation of both the J and V time series.

[11] Given the set of event days, t_E, and event-forecasted days, t_F, from the above analysis, we define the number of correct forecasts to be the number of t_F values for which there is one or more t_E in the interval $t_F \leq t \leq t_F + 2$, so that the forecast of an event is extended over 3 days.

[12] As noted in section 1, in many applications one is interested in knowing if a key quantity crosses a threshold value. If this is the case, the quality of the binary forecast can be analyzed by the 2 × 2 contingency table shown in Table 1. There are many possible ratios that can be derived from this table, but in this work we focus on the two which are most relevant from a user's perspective: the forecast ratio and the likelihood ratio.

[13] The forecast ratio can be used to determine if a forecast algorithm has economic utility if mitigating action is taken every time a forecast is made. If we assume that (1) the forecast is always followed and (2) always forecasting an event yields a net loss, then this ratio is the number of correct forecasts ("Hits") to the number of false alarms forecasts [*Matthews*, 1997; *Thomson*, 2000; *Wilks*, 2001]. We label this ratio the forecast ratio $R_F \equiv N_H/N_{\overline{H}}$. The ratio follows from the restriction that the utility $U = BN_H - CN_{\overline{H}}$ is positive, where B is the net monetary benefit from having taken mitigating action based on a correctly forecasted event and C is the cost when action is taken but no event occurs. Because the two parameters C and B are system-dependent, the ratio R_F computed here should be considered as a a minimum usefulness ratio. Moreover, if C and B are known and $R_F > C/B$, then the forecast algorithm is useful, and further evaluation of the algorithm should seek to maximize U.

Table 1. Contingency Table With Notation Used in Text[a]

	Observed		
Forecast	Yes	No	Total
Yes	N_H	$N_{\overline{H}}$	$N_F = N_H + N_{\overline{H}}$
No	N_M	x	$N_{\overline{F}} = N_M + x$
Total	$N_E = N_H + N_M$	$N_{\overline{E}} = N_{\overline{H}} + x$	N

[a] N_H is the number of correct forecasts, $N_{\overline{H}}$ is the number of false alarms, N_M is the number of events that were not predicted, and x represents the number of intervals with no forecasts or events. The total number of forecasts is N_F, while the total number of time intervals without a warning is $N_{\overline{F}}$. Both $N_E + N_{\overline{E}}$ and $N_F + N_{\overline{F}}$ sum to N, the total number of warning plus nonwarning intervals. N may be less than the number of points in the time series because forecasts are extended over 3 days.

[14] The second key metric is the likelihood ratio LR $\equiv P(F|E)/P(F|\overline{E})$, where the numerator is the probability of a forecast given an event occurred and the denominator is the probability of a forecast given that there was no event. From Table 1, LR = $(N_H/N_{\overline{H}})(N_{\overline{H}} + x)/(N_H + N_M) = (N_H/N_{\overline{H}})(N_{\overline{E}}/N_E)$. If the odds of an event, given by the ratio $N_E/N_{\overline{E}}$, is stationary, then maximizing R_F is equivalent to maximizing LR. If $LR > 1$, then the forecast has merit in the sense that it is better than a coin-flip forecast algorithm, for which $LR = 1$ [*Matthews*, 1997]. Note that the restriction $LR > 1$ also follows if we demand that an "always forecast event" algorithm has $U \leq 0$ and the considered forecast algorithm has U > 0.

[15] As an example of the computations of these two ratios, consider Figure 1, which shows part of the two time series from which the number of correct forecasts is computed. In this time window, there are three forecasts. There are three events in this interval, two of which were forecasted according the algorithm. Thus the number of events in J is $N_E = 3$, while the number of forecasts is $N_F = 3$. The number of correct forecasts is $N_H = 2$, and the number of false alarms is $N_{\overline{H}} = 1$, giving $R_F = 2$, while $LR = 37.3$.

[16] For the algorithm given by equation 2, there are two adjustable threshold parameters: V_c and J_c. Figure 2 shows the R_F statistic computed using the full data set of daily averaged V_{SW} and J_e (1950 days) as a function of the two parameters. To prevent solutions for which a small number of forecasts are made, we set $R_F = 0$ at points where $N_F < 20$.

[17] The forecast ratio, R_F, has a strong dependence on the two threshold parameters. The lower limit of $J_c = 1$ corresponds to a value of J_e for which 53% of the measurements are below. Values of J above this value were chosen to represent the "large-event" population. The optimal choice of parameters is a large value (with respect to $V_{ave} = 0.28$) of V_c for values of $J_c \geq 1$. The maximum value

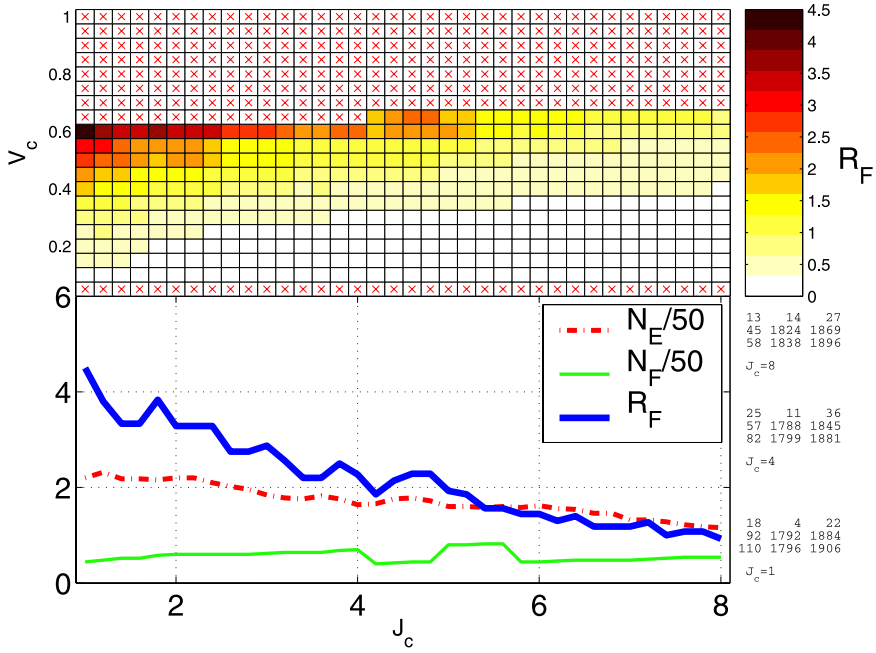

Figure 2. Forecast quantities as a function of the threshold parameters [V_c, J_c]. For $J = 1$, the peak is located at $V_c = 0.6$, which corresponds to $V_{sw} = 600$ km/sec. Locations where $N_F < 20$ are marked with crosses.

of R_F is 4.4; the algorithm correctly predicted 18 events, while 4 forecasts were made after which no event occurred. The curves shown in the lower panel correspond to the largest value of R_F with respect to V_c and show the number of forecasts and events at the optimal value of V_c. Contingency tables for three select values of J_c are shown the right side of Figure 2.

[18] Although the algorithm is most often correct when a forecast is issued, many events went unpredicted. At $J_c = 1$, there were 92 events for which no forecast was issued. As noted earlier, from an practical standpoint this failure mode is probably of less importance than that given by the ratio R_F. From a modeling perspective, there are many possible interpretations for a model that is almost always correct when it makes a prediction but still misses many events. One interpretation is that J_e events are driven by several processes, one of which is always active when V_{sw} is very large while the unpredicted events are driven by a process with a component that is independent of large V_{sw}.

[19] The simple threshold model was motivated by the observation that elevated values of solar wind velocity are associated with large-flux events. To give this observation an interpretation in terms of probability densities, Figure 3 shows the scatter diagram of the daily averaged velocity data. The prediction region corresponding to equation 2 is shown by the rectangle in the lower right section of Figure 3. When a point appears in the area enclosed by this region, a prediction of a large-flux event is made. For each [$V(t-1)$, $V(t-2)$] pair, a marker is shown to label the day that J first crossed the threshold value of $J_c = 1$.

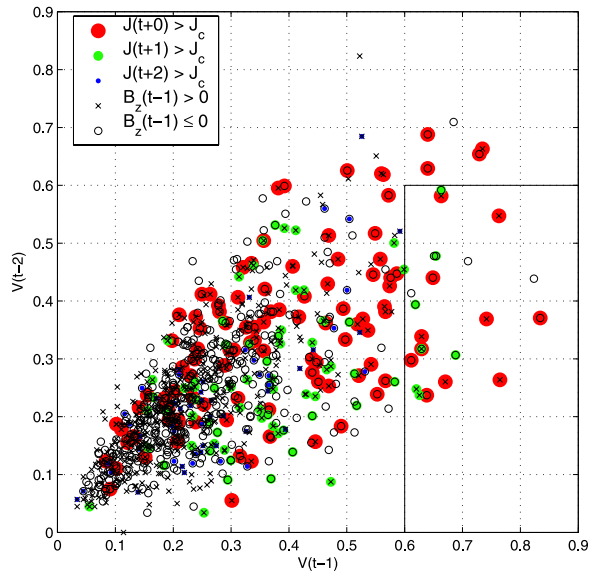

Figure 3. All combinations of consecutive velocity measurements for which $J(t-1) \leq J_c$ are labeled with crosses if $B_z(t-1) > 0$ or o if $B_z(t-1) \geq 0$. Combinations of velocities for which a threshold crossing in J above $J_c = 1$ first occurred on day t, $t+1$ or $t+2$ are also shown. The rectangular area represents the prediction region of equation 2. In this area, $N_H = 18$ and $N_{\overline{H}} = 4$ giving $R_F = 4.4$.

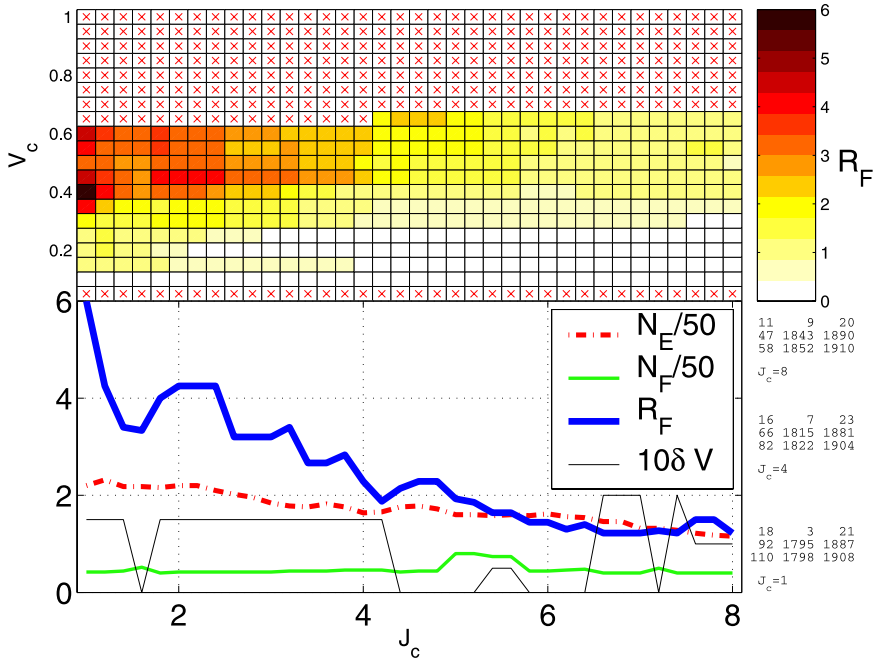

Figure 4. Forecast quantities as a function of the threshold parameters V_c, and J_c. For J_c = 1, the peak is located at V_c = 0.4, which corresponds to V_{sw} = 487 km/sec.

[20] From Figure 3, it is clear that although there is much overlap of the events with the nonevents, there are regions where more events would have been predicted. In two dimensions (two V-lags), the problem of optimizing R_F is equivalent to finding a region (or regions) on this scatterplot that yields the highest value of R_F or the lowest amount of overlap of the probability density of N_H and $N_{\overline{H}}$. The restriction that $N_F \geq 20$ is equivalent to stating that the number of points enclosed by the prediction region is greater than or equal to 20.

[21] In the case of event forecasting the number of data points that we are fitting the model to is the actual number of forecasts, as opposed to the number of points in the full time series. To prevent over fitting, the number of free parameters must be much smaller than the number of forecasts. As an example, consider replacing the simple rectangular decision region in Figure 3 with a complex boundary so that 20 events are within the boundary and no nonevents are within it. If the number of parameters that it takes to describe the shape is on the order of 20, then it is likely that the shape is a result of over fitting.

[22] It has been noted that the processes present during geomagnetic storms and substorms may also contribute to the appearance of energetic electrons (see review by *Friedel et al.* [2002]). Because both storms and substorms are driven primarily by a reconnection solar wind quantity, $V_{sw}B_s$, we can test the value of the daily average of B_z as a proxy for the existence of storms or substorms. The values of $[V(t-1), V(t-2)]$ in Figure 3 are coded by the average value of B_z on day $t-1$. For both the events and the nonevents in the prediction rectangle, there are approximately equal numbers of positive B_z and negative B_z averages on the previous day. This indicates that the daily average value of B_z is not a good separator of events from nonevents. It is likely that the behavior of B_z does contain additional precursor information on subdaily times scales, from which a better substorm or storm proxy can be derived, such as the time integral of B_s.

[23] Another example of a precursor indicator is ULF activity [*Rostoker et al.*, 1998; *Mathie and Mann*, 2000]. *O'Brien et al.* [2001] has shown an association (in terms of an epoch time series centered on the peak of a geomagnetic storm) between energetic electron activity and elevated ULF power 24 hours before and after the peak of a magnetic storm. This indicates that ULF wave power may have a significant value as a precursor. One strong driver of ULF activity in the magnetosphere is due to the Kelvin-Helmholtz instability [*Southwood*, 1968], which is in turn driven by elevated solar wind velocity [*Vennerstrøm*, 1999]. Because ULF activity is not completely predictable from solar wind measurements, it is likely that ULF activity will provide information that will improve large-event forecasts, although this would be at the expense of reduced lead time. The analysis of non-SW precursors and subdaily timescales will be considered in a future work.

[24] By visual inspection, the lower right quadrant of Figure 3 has a high ratio of events (indicated by a colored dot) to nonevents (indicated by an x or o with no colored dot). Physically, this means that if there is a jump in the daily averaged solar wind velocity over one day, an event often followed on one of the next three days. Such a jump in the daily averaged data can exist for many reasons,

including a slow rise over the full day to a steep increase over a short timescale due to a tangential discontinuity. The present model does not distinguish between such possibilities. Expanding the first model to allow for such a prediction region gives a second model

$$V(t-1) \geq V_{c1} \text{ and } V(t-2) < V_{c2} \text{ and } J(t-1) < J_c. \quad (3)$$

For this model the optimization is with respect to 2 parameters, V_{c1} and V_{c2}. Figure 4 shows the result of evaluating R_F with the same grid resolution as used for Figure 2.

[25] The analysis of the jump model yields slightly improved values of R_F. Comparison of the contingency tables for the threshold and jump models at J_c = 1 shows that their elements are nearly the same; the jump model had one fewer false alarm. The significance in this improvement is small because the model with one additional parameter yielded only a change in one data point. At higher values of J_c, the jump model also slightly outperforms the threshold model in terms of the maximum value of R_F. It can be concluded that a jump in the solar wind velocity can yield slightly higher ratios of R_F for certain values of J_c, but such jumps have little additional information in comparison to knowledge of only a threshold crossing.

3. L Shell Dependence of R_F

[26] Energetic electrons are known to have a response to the solar wind that is highly dependent on L shell. Figure 5 shows that the performance of the threshold algorithm also has a strong L shell dependence. In Figure 5a, the optimal value of $R_F(J_c, V_c)$ with J_c values ranging from 1 to 8 is plotted. (In general, the maximum value of R_F occurs for low J_c, which is expected from the R_F curves shown in Figures 2 and 4.) Figures 5b–5d show the same result as 5a, except the grid of J_c values considered includes values above 0.1, 0.01, and.001, which correspond to fluxes that exceed 100, 10, and 1 particle/str·cm^2·s, respectively.

[27] At the largest flux threshold, nonzero values of R_F are found in the L shell range of [3, 5.6], as shown in Figure 5a. For nearly all L shells the optimal value of V_c is 0.6, corresponding to V_{sw} = 600 km/s. The peak occurs at L = 4.7, where the number of forecasts was 27, of which 3 were incorrect. As was the case for L = 4.4, many events went unpredicted, as evidenced by the ratio of N_E/N_F = 4.6.

[28] Figures 5b–5d shows that if we change the value defining a large energetic electron event to be smaller by factors of 10, several new features are revealed. First is the appearance of L shells for which every prediction was correct. Second, the R_F ratios substantially increase (note the change in scale). Finally, the region of elevated R_F shifts toward higher L shells. The shift is due to the fact that as the threshold value of J is decreased, there is an increasing number of events. At the very low threshold of J_c = 0.001 (Figure 5d), corresponding to J_e = 1 particle/str·cm^2·s, the region between L = 4–4.8 has zero R_F. This is a result of J_e rarely crossing below the threshold so that the number of forecasts is not above 20. Also, the optimal velocity threshold is lower between L = 4.8–5.6, with typical values of 400 km/s.

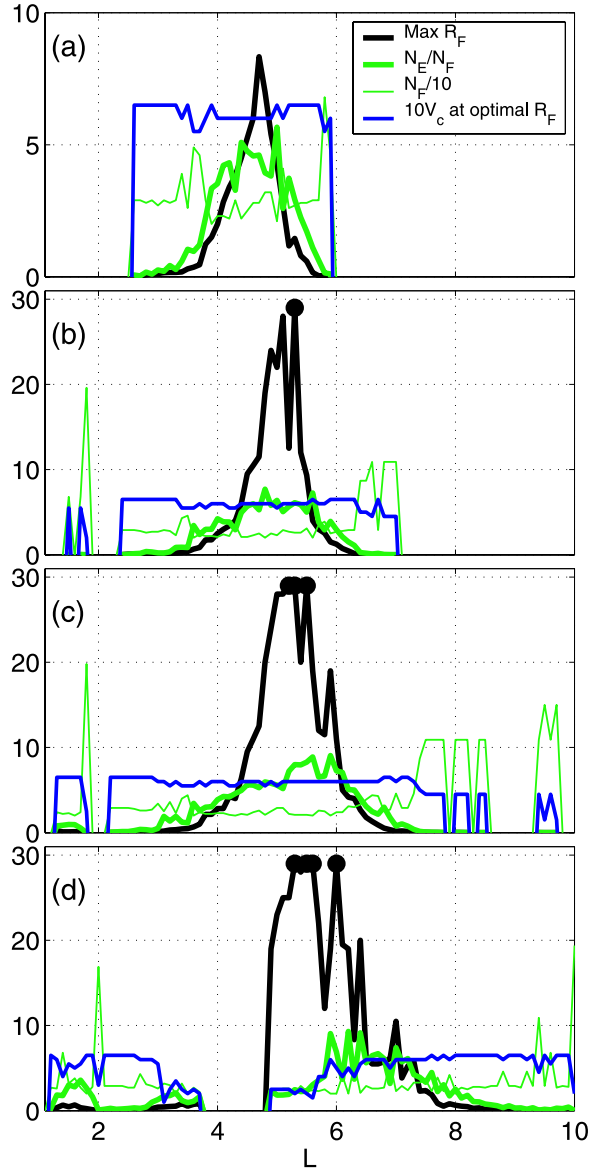

Figure 5. Maximum forecast metric R_F as a function of L shell for different lower limits of critical flux J_c with (a) J_c = 1, (b) J_c = 0.1, (c) J_c = 0.01, and (d) J_c = 0.001. These scaled values of flux correspond to J_e values of 1000, 100, 10, and 1 particles/str·cm^2·s, respectively. R_F values were calculated for each L shell on the V_c grid used in Figure 2. Again we have considered values of R_F for which $N_F \geq 20$.

[29] From Figure 5, we conclude that at certain L shells and flux threshold levels, a transition in the daily averaged solar wind velocity from below to above 600 km/s is a sufficient condition for an increase in the relativistic elec-

tron fluxes above a threshold value, provided that the flux initially below this threshold.

4. Discussion and Conclusions

[30] Large-amplitude relativistic electron flux events have been implicated in causing disturbances that upset satellite systems and have a component that is driven by high-speed solar wind streams, which have a characteristic velocity profile. Although on average a characteristic velocity profile generally precedes electron events, such characteristic velocity profiles do not always lead to a high-flux event. Seeking to evaluate how useful the characteristic velocity profile is as a precursor, we have developed a model that both statistically quantifies the association and can be used to forecast large-amplitude relativistic electron fluxes. The methodology is easily extended to subdaily timescales and quantities that are better proxies for satellite interruptions, e.g., the integrated flux.

[31] A threshold model, which predicts an electron event when the daily averaged solar wind velocity crosses a threshold value, predicted 18 events and had 4 false alarms for a velocity threshold of 600 km/sec at L = 4.4. For this J threshold value, 110 events occurred. A generalized threshold model which allowed for a jump in the daily averaged solar wind velocity to be a large-event predictor yielded slightly increased maximum R_F ratios. Most of the improvement was observed for large values of J_c.

[32] The threshold model was also analyzed for L = [1.1, 10]. It was shown that at thresholds at or below 100 particles/str·cm^2·s there were many locations where very few predictions were made after which no event occurred. We interpret this as an indication that large-amplitude fluxes may be driven by a process that is activated by (and derivable from) large V_{sw} only. To verify this, one would have to show that any other drivers did not simultaneously appear with every V_{sw} event. Approximately 80% of large-amplitude events were not predicted by the threshold model. This indicates that these events may have been activated by a process not completely derivable from daily averaged values of V_{sw} alone.

[33] The approach and methods developed in this work are a form of pattern recognition and can be further generalized both by using a classification and density approximation formalism (e.g., *Silverman* [1986]) and by determining the optimal prediction regions in higher dimensions (i.e., with more V_{sw}-lags and with other possible precursor variables). With this more general approach, precursor indicators other than V_{sw} can be systematically tested.

[34] **Acknowledgments.** We thank S. G. Kanekal for providing the processed SAMPEX data. IMF and ion velocity data were obtained from the OMNI database at NSSDC.

References

Baker, D., R. Belian, P. Higbie, R. Klebesadel, and J. Blake, Deep dielectric charging effects due to high-energy electrons in earth's outer magnetosphere, *J. Electrost.*, *20*, 3–19, 1987.

Baker, D., et al., Recurrent geomagnetic storms and relativistic electron enhancements in the outer magnetosphere: ISTP coordinated measurements, *J. Geophys. Res.*, *102*, 14,141–14,148, 1997.

Baker, D. N., R. L. McPherron, T. E. Cayton, and R. W. Klebesadel, Linear prediction filter analysis of relativistic electron properties at 6. 6 R_e, *J. Geophys. Res-Space Phys.*, *95*, 15,133–15,140, 1990.

Baker, D. N., X. Li, J. B. Blake, and S. Kanekal, Strong electron acceleration in the Earth's magnetosphere, *Adv. Space Res.*, *21*, 609–613, 1998.

Blake, J. B., D. N. Baker, N. Turner, K. W. Ogilvie, and R. P. Lepping, Correlation of changes in the outer-zone relativistic-electron population with upstream solar wind and magnetic field measurements, *Geophys. Res. Lett.*, *24*, 927–929, 1997.

Friedel, R. H. W., G. D. Reeves, and T. Obara, Relativistic electron dynamics in the inner magnetosphere: A review, *J. Atmos. Terr. Phys.*, *64*, 265–282, 2002.

Li, X. L., M. Temerin, D. N. Baker, G. D. Reeves, and D. Larson, Quantitative prediction of radiation belt electrons at geostationary orbit based on solar wind measurements, *Geophys. Res. Lett.*, *28*, 1887–1890, 2001.

Mathie, R. A., and I. R. Mann, A correlation between extended intervals of ULF wave power and storm-time geosynchronous relativistic electron flux enhancements, *Geophys. Res. Lett.*, *27*, 3261–3265, 2000.

Matthews, R., Decision-theoretic limits on earthquake prediction, *Geophys. J. Int.*, *131*, 526–529, 1997.

O'Brien, T. P., R. L. McPherron, D. Sornette, G. D. Reeves, R. Friedel, and H. J. Singer, Which magnetic storms produce relativistic electrons at geosynchronous orbit?, *J. Geophys. Res.*, *106*, 15,533–15,544, 2001.

Rostoker, G., S. Skone, and D. N. Baker, On the origin of relativistic electrons in the magnetosphere associated with some geomagnetic storms, *Geophys. Res. Lett.*, *25*, 3701–3705, 1998.

Silverman, B., ***Density Estimation for Statistics and Data Analysis***, Chapman and Hall, New York, 1986.

Southwood, D., Hydromagnetic stability of magnetospheric boundary, *Planet Space Sci.*, *16*, 587, 1968.

Thomson, A., Evaluating space weather forecasts of geomagnetic activity from a user perspective, *Geophys. Res. Lett.*, *27*, 4049–4052, 2000.

Vampola, A., Thick dielectric charging on high-altitude spacecraft, *J. Electrost.*, *20*, 21–30, 1987.

Vassiliadis, D., A. J. Klimas, S. Kanekal, D. Baker, and R. S. Weigel, Long-term-average, solar-cycle, and seasonal response of magnetospheric energetic electrons to the solar wind speed, *J. Geophys. Res.*, *107*(A11), 1383, doi:10.1029/2001JA000506, 2002.

Vassiliadis, D., R. S. Weigel, A. Klimas, S. Kanekal, and R. Mewaldt, Modes of energy transfer from the solar wind to the inner magnetosphere, *Phys. Plasmas*, *10*, 463–473, 2003.

Vennerstrøm, S., Dayside magnetic ULF power at high latitudes: A possible long-term proxy for the solar wind velocity?, *J. Geophys. Res.*, *104*, 10,145–10,157, 1999.

Wilks, D., A skill score based on economic value for probability forecasts, *Meteorol. Appl.*, *8*, 209–219, 2001.

A. J. Klimas, NASA Goddard Space Flight Center, Greenbelt, MD 20771, USA.

D. Vassiliadis, Universities Space Research Association at NASA Goddard Space Flight Center, Greenbelt, MD 20771, USA.

R. S. Weigel, Laboratory for Atmospheric and Space Physics, University of Colorado, Boulder, CO 80303, USA. (robert.weigel@lasp.colorado.edu)